

# Mid-Infrared Spectroscopic Properties of Ultra-Luminous Infrared Quasars

Chen Cao,<sup>1,2,3,4\*</sup> X. Y. Xia,<sup>5†</sup> Hong Wu,<sup>3</sup> S. Mao,<sup>6,5</sup> C. N. Hao,<sup>7,5</sup> Z. G. Deng<sup>4,5,3</sup>

<sup>1</sup>*School of Space Science and Physics, Shandong University at Weihai, Weihai, Shandong 264209, China*

<sup>2</sup>*Visiting Scholar, Harvard-Smithsonian Center for Astrophysics, Cambridge, MA 02138*

<sup>3</sup>*National Astronomical Observatories, Chinese Academy of Sciences, Beijing 100012, China*

<sup>4</sup>*Graduate University, Chinese Academy of Sciences, Beijing 100039, China*

<sup>5</sup>*Tianjin Astrophysics Center, Tianjin Normal University, Tianjin 300384, China*

<sup>6</sup>*Jodrell Bank Centre for Astrophysics, Alan Turing Building, University of Manchester, Manchester M13 9PL, UK*

<sup>7</sup>*Institute of Astronomy, University of Cambridge, Madingley Road, Cambridge CB3 0HA, UK*

1 September 2021

## ABSTRACT

We analyse mid-infrared (MIR) spectroscopic properties for 19 ultra-luminous infrared quasars (IR QSOs) in the local universe based on the spectra from the Infrared Spectrograph on board the *Spitzer Space Telescope*. The MIR properties of IR QSOs are compared with those of optically-selected Palomar-Green QSOs (PG QSOs) and ultra-luminous infrared galaxies (ULIRGs). The average MIR spectral features from  $\sim 5$  to  $30\mu\text{m}$ , including the spectral slopes,  $6.2\mu\text{m}$  PAH emission strengths and [NeII]  $12.81\mu\text{m}$  luminosities of IR QSOs, differ from those of PG QSOs. In contrast, IR QSOs and ULIRGs have comparable PAH and [NeII] luminosities. These results are consistent with IR QSOs being at a transitional stage from ULIRGs to classical QSOs. We also find that the colour index  $\alpha(30, 15)$  is a good indicator of the relative contribution of starbursts to AGNs for all QSOs. Correlations between the [NeII]  $12.81\mu\text{m}$  and PAH  $6.2\mu\text{m}$  luminosities and those between the [NeII], PAH with  $60\mu\text{m}$  luminosities for ULIRGs and IR QSOs indicate that both [NeII] and PAH luminosities are approximate star formation rate indicators for IR QSOs and starburst-dominated galaxies; the scatters are, however, quite large ( $\sim 0.7$  to  $0.8$  dex). Finally the correlation between the EW (PAH  $6.2\mu\text{m}$ ) and outflow velocities suggests that star formation activities are suppressed by feedback from AGNs and/or supernovae.

**Key words:** galaxies: active – galaxies: evolution – galaxies: interactions – quasars: general — infrared: galaxies

## 1 INTRODUCTION

Since the discovery of ultra-luminous infrared galaxies (ULIRGs,  $L_{\text{IR}} > 10^{12} L_{\odot}$ ) by the *Infrared Astronomical Satellite* (IRAS) in the 1980's (e.g., Houck et al. 1985), it is widely accepted that ULIRGs result from strong interactions/mergers between gas-rich disk galaxies. These mergers form elliptical galaxies and ULIRGs are an important intermediate stage in the process during which at least a fraction of ULIRGs manifest as dust-enshrouded QSOs (see, e.g., Sanders & Mirabel 1996; Lonsdale et al. 2006). In addition, active galactic nuclei (AGNs) triggered by mergers tend to appear at the final merging stages (e.g., Sanders et al. 1988,

Zheng et al. 1999, Cui et al. 2001, Veilleux et al. 2002 and reference therein).

There is mounting evidence that QSOs with far-infrared (FIR) excess have massive starbursts in their host galaxies. For example, Canalizo & Stockton (2001) investigated 9 QSOs with FIR excess and found that their host galaxies are tidally interacting or major merger systems with obvious recent star-forming activities. From the detections of mid-infrared (MIR)/FIR<sup>1</sup> emissions for FeLoBALs (Broad Absorption Line QSOs with low-ionisation and iron absorption lines) by Multiband Imaging Photometer on *Spitzer* (MIPS; Rieke et al. 2004) on board the *Spitzer Space Telescope* (Werner et al. 2004), Farrah et al. (2007a) find that all

\* E-mail: ccao00@gmail.com

† E-mail: xyxia@bao.ac.cn

<sup>1</sup> In this paper, MIR refers to  $5\text{--}35\mu\text{m}$ , FIR  $35\text{--}350\mu\text{m}$ , and IR  $8\text{--}1000\mu\text{m}$ .

their 9 FeLoBALs are extremely infrared (IR) bright, and concluded that these QSOs are in transition from ULIRGs to classical QSOs with ongoing or recent starbursts, because the iron absorption may be from iron ejected during starbursts. Hao et al. (2005a) studied 31 QSOs/Seyfert's 1s selected from the local ULIRG samples (termed as IR QSOs for simplicity). By comparing the FIR spectral index of IR QSOs with those of optically selected Palomar-Green QSOs (PG QSOs; Schmidt & Green 1983), they argued that the FIR excess of IR QSOs relative to PG QSOs is from massive starbursts and inferred star formation rate (SFR) in the host galaxies of IR QSOs. Recently, from studies of  $z \sim 6$  QSOs with strong sub-mm emissions, Carilli et al. (2007), Wang et al. (2007) and Wang et al. (2008) concluded that massive starbursts also exist in their host galaxies. The conclusion is consistent with the results of Hao et al. (2008) that high redshift (sub)mm-loud QSOs follow the same trend for FIR to bolometric luminosities established by low redshift IR QSOs (Hao et al. 2005a). All these studies suggest that there exists a transitional stage, during which both the central black hole and the spheroidal component of QSO hosts grow rapidly in a coeval fashion.

However, there is still a debate about the origin of FIR emission from QSOs, because one cannot firmly exclude the possibility that FIR emissions are from dust tori heated by central AGNs (for detailed discussions see Haas et al. 2003). Moreover, from the molecular gas properties of PG QSOs with IR excess and comparisons with ULIRGs, Evans et al. (2006) find that the  $L_{\text{IR}}/L'_{\text{CO}}$  and  $L_{\text{IR}}/L'_{\text{HCN}}$  ratios for PG QSOs are higher than those of ULIRGs, implying that AGNs contribute significantly to the dust heating and hence to the FIR emission. Therefore, other SFR indicators besides the FIR emission for QSOs are important for further understanding the coeval growth of supermassive black holes and their host galaxies.

Recently, the QUEST (Quasar and ULIRG Evolution Study) group (see Schweitzer et al. 2006; Netzer et al. 2007) reported the detection of polycyclic aromatic hydrocarbon (PAH) emission features in PG QSOs using the Infrared Spectrograph (IRS) on *Spitzer* (Houck et al. 2004). For 11 out of 26 PG QSOs PAHs have been clearly detected. Furthermore, the average spectrum of the undetected 15 PG QSOs also shows PAH features. Since the PAH emissions are closely related to star formation, not to AGNs (see, e.g., Shi et al. 2007), such detections strongly suggest that star formation occurs widely in QSOs. Their analysis shows that 30% or more FIR emission in these PG QSOs is from starbursts. Furthermore, given that the low-excitation fine-structure emission line [NeII]  $12.81\mu\text{m}$  is one of the dominant emission lines of HII regions and that the PAH molecules are easily destroyed by high energy photons from AGNs (e.g., Wu et al. 2007), [NeII] emission may be an alternative, perhaps even better, tracer of star formation for QSOs (see §4).

In this paper we study the MIR spectroscopic properties of IR QSOs based on *Spitzer* IRS observations, and examine their connections and evolutionary relations to ULIRGs and PG QSOs. The sample selection, data acquisition and reduction are described in Sect. 2 and 3. The major results and discussions are given in Sect. 4 and 5. Finally we summarise our results in Sect. 6. We adopt cosmological parameters  $H_0 = 70 \text{ km s}^{-1} \text{ Mpc}^{-1}$ ,  $\Omega_m = 0.3$ , and  $\Omega_\Lambda = 0.7$  throughout this paper.

## 2 SAMPLE SELECTION

IR QSOs are defined as type 1 AGN with  $L_{\text{IR}}(8 - 1000\mu\text{m}) > 10^{12} L_\odot$  (Zheng et al. 2002). Our basic IR QSO samples are compiled from ULIRG samples with spectroscopic information, plus the IR QSOs obtained directly from the cross-correlation of the *IRAS* Point-Source catalog with the *ROSAT* All-Sky Survey Catalog. The ULIRG samples consist of 118 ULIRGs from 1 Jy ULIRGs survey (Kim & Sanders 1998) and 97 ULIRGs from the QDOT redshift survey (Lawrence et al. 1999). The total number of IR QSOs is 31, about one third of all the IR QSOs found in a complete redshift survey with 15,411 *IRAS* galaxies and about 900 ULIRGs (PSCz; Saunders et al. 2000). Thus it should be a representative sample of IR QSOs (see Zheng et al. 2002 and Hao et al. 2005a for more detailed descriptions).

We searched the *Spitzer* archival data and found that 18 out of 31 IR QSOs have been observed by IRS and the data are available (see Table 1). Notice that 9 of the 10 IR QSOs (out of a total of 118 ULIRGs) from the 1 Jy ULIRG sample are included in our sample. The other 9 IR QSOs are from QDOT (4) and other QSO samples. In addition we include the object IRAS F14026+4341, which is classified as a hyper-luminous infrared galaxy (with  $L_{\text{FIR}} > 10^{13} L_\odot$ , Rowan-Robinson 2000) and a broad absorption line quasar (Low et al. 1989). Our sample includes 90% (50%) IR QSOs out of 1 Jy (QDOT) ULIRGs, and thus should be an overall representative sample. We checked that our results are essentially unchanged if we focus only on the 9 IR QSOs from the 1 Jy ULIRG samples, and thus our compiled sample has no significant biases.

14 of the 19 objects have both low- and high-resolution IRS observations, while four (3C 48, IRAS F02054+0835, PG 1543+489, and IRAS F20036-1547) have only low-resolution observations, and one (IRAS F21219-1757) has no Long-Low (LL) mode (see §3.1) observation (see Table 3).

The IRS low-resolution spectra of a sample of Palomar-Green QSOs (PG QSOs) are retrieved from *Spitzer* GTO and GO archival data (programs 14, 3187, 3421, and 20142; see Table 4). We remove objects whose MIR spectra have a low S/N ratio or redshift larger than 0.27 to guarantee reliable measurements of rest-frame  $30\mu\text{m}$  fluxes. The number of PG QSOs is 19 (see Table 1), the same as the number of IR QSOs. This PG QSO sample is mainly used for studying the MIR spectral slopes benefiting from the full wavelength coverage from  $\sim 5\text{--}30\mu\text{m}$  of their low-resolution spectra. We also collected another PG QSO sample with 22 objects studied by Schweitzer et al. (2006) (after excluding four objects that have been classified as IR QSOs and grouped into IR QSO sample). This second PG QSO sample has deep SL mode observations ( $5.2\text{--}14.5\mu\text{m}$ ) and is thus suitable for studying weak PAH emission features in continuum-dominated QSOs, and for analysing properties of the MIR fine-structure lines (especially [NeII]  $12.81\mu\text{m}$  line in this work) from high-resolution observations.

The sample of Ultra-Luminous Infrared Galaxies (ULIRGs) is selected based on the *IRAS* 1 Jy sample of ULIRGs (Kim & Sanders 1998), which have optical spectroscopic observations by Veilleux et al. (1999) and Wu et al. (1998). Their IRS low-resolution spectra are retrieved from *Spitzer* GTO archival data (program ID 105; see Table 4).

The number in our ULIRG sample is 35 (see Table 2), including all spectral types except type 1 AGNs, namely Seyfert 2's, LINERs, and HIIs as classified by Veilleux et al. (1999) and Wu et al. (1998) from diagnostic diagrams of optical lines.

### 3 DATA ACQUISITION AND REDUCTION

#### 3.1 Mid-infrared spectra from *Spitzer* IRS

The MIR spectra are acquired from the *Spitzer* archival data using the Leopard software (see Table 3 for the integrated exposure times and program IDs for IR QSOs). The data (versions 13.2 to 15.3 of *Spitzer* pipeline reduction) include low-resolution (Short-Low [SL] & Long-Low [LL] modes,  $R \sim 60$ -120 and wavelength range:  $5.2$ - $38.0 \mu\text{m}$ ) IRS spectra for IR QSOs, PG QSOs, and ULIRGs, and high-resolution (Short-High [SH] & Long-High [LH] modes,  $R \sim 600$  and wavelength range:  $9.9$ - $37.2 \mu\text{m}$ ) IRS spectra for most of the IR QSOs. We use the SMART software (Higdon et al. 2004) for data reduction, including the removal of rogue pixels, sky subtraction, and spectral extraction and analysis. The sky backgrounds for low-resolution (SL & LL modes) spectra are subtracted by differencing the adjacent sub-slit positions (1st & 2nd nods). No background subtraction is performed for the high-resolution (SH & LH modes) spectra, but this does not affect MIR fine-structure line measurements (see, e.g., Farrah et al. 2007b). The slit widths of  $3''.6$  to  $11''.1$  include most of the emission from the QSO and its host galaxy, so no aperture corrections are performed. For the low-resolution spectra we use the  $12 \mu\text{m}$  and  $25 \mu\text{m}$  flux densities from *IRAS* (or *ISO* if the *IRAS* fluxes are upper limits or not available) to scale the spectra by multiplying by a small factor, which is more suitable for the comparison between MIR and FIR properties in our statistics. The scaling factors for IR QSOs and ULIRGs are often close to unity, typically less than 1.1<sup>2</sup>. However, for PG QSOs the scaling factors are larger, typically  $\sim 1.5$ . This may be caused by variabilities of quasars in MIR (e.g., Neugebauer & Matthews 1999) and/or contamination of companions (environments) for *IRAS* (or *ISO*) measurements.

#### 3.2 Measurements of PAH and mid-infrared fine-structure lines

The fluxes of PAH emission at  $6.2 \mu\text{m}$  are measured by integrating the flux above a local continuum from  $6.0$ - $6.5 \mu\text{m}$  approximated by a second-order polynomial (e.g., Spoon et al. 2007; Desai et al. 2007). The uncertainties ( $1\sigma$ ) in the measurements are 20% on average (varying from  $\sim 5\%$  for PAH strong objects to about 50% for those with only marginally detectable PAH features). The equivalent widths (EW) of  $6.2 \mu\text{m}$  PAH feature are obtained from dividing the integrated PAH flux by the continuum flux density below the peak of the feature. Upper limits ( $3\sigma$ ) are given by adopting typical widths of  $\sim 0.2 \mu\text{m}$  for the  $6.2 \mu\text{m}$  PAH feature

(Smith et al. 2007), which is similar to the value,  $\sim 0.6 \mu\text{m}$ , used for the  $7.7 \mu\text{m}$  feature by Schweitzer et al. (2006).

Note that we do not fit Gaussian or Lorentzian profiles to measure PAH emissions (e.g., Schweitzer et al. 2006; Imanishi et al. 2007) due to the relative weakness of PAH features in QSOs compared to their strong dust continuum. Since the three IR QSOs in the QUEST sample (I Zw 1, Mrk 1014, PG 1613+518) have 7.7/6.2 flux ratios of 4.2, 4.6, 4.9, respectively, similar to that of NGC 6240 (4.7, Armus et al. 2006), we estimate the  $6.2 \mu\text{m}$  PAH fluxes for PG QSOs in the Schweitzer et al. (2006) sample (which has only  $7.7 \mu\text{m}$  measurements) by taking a 7.7/6.2 flux ratio of 4.7.

The fluxes of the ionised neon fine-structure lines in the MIR ([NeII], [NeV], [NeIII] at  $12.81$ ,  $14.32$ , and  $15.56 \mu\text{m}$ ) for IR QSOs are measured based on the high-resolution IRS spectra, using the IDEA spectral analysis tool of the SMART software. The fluxes are measured by fitting a single Gaussian superposed on a local continuum approximated by a second-order polynomial. Flux upper limits ( $3\sigma$ ) are derived adopting typical line widths of  $600 \text{ km s}^{-1}$  (Schweitzer et al. 2006). The fluxes of the [NeII] $12.81 \mu\text{m}$  line for some ULIRGs in our sample are from Farrah et al. (2007b).

### 4 RESULTS

#### 4.1 Mid-infrared spectral characteristics of IR QSOs

Fig. 1 shows the low-resolution *Spitzer* IRS MIR spectra of 18 IR QSOs in our sample (except IRAS F21219-1757 which has no LL mode observation). The dotted and dashed lines show the PAH features and the MIR fine-structure neon, sulphur, and oxygen lines. The shaded bar denotes the silicate emission/absorption feature centred at  $9.7 \mu\text{m}$ . One can see from these spectra that the PAH features at  $6.2$ ,  $7.7$ ,  $8.6$ ,  $11.2$  &  $12.7 \mu\text{m}$  and the MIR fine-structure emission lines, such as [NeII]  $12.81 \mu\text{m}$ , [NeV]  $14.32 \mu\text{m}$ , [NeIII]  $15.56 \mu\text{m}$ , [NeV]  $24.32 \mu\text{m}$  & [OIV]  $25.89 \mu\text{m}$  are present in most IR QSOs, although some emissions are weak for most of them. One can also see the silicate absorption feature at  $9.7 \mu\text{m}$  for several IR QSOs (F00275, F13218, Mrk 231, F11119 and F15462), which are rarely seen in PG QSOs. For comparison, we show the average MIR spectra of IR QSOs, PG QSOs and ULIRGs in Fig. 2. The average spectra of ULIRGs and PG QSOs are from Hao et al. (2007). It is clear from Fig. 2 that the slope of MIR continua from  $15 \mu\text{m}$  to  $30 \mu\text{m}$  of IR QSOs is intermediate between that of ULIRGs and QSOs. We also show in the same figure the spectra of two representative IR QSOs (PG 1613+658 and Mrk 231). Their MIR spectra are intermediate between the average spectra of ULIRGs and PG QSOs. However, from the infrared, optical and X-ray observations, PG 1613+658 has the characteristics of classical QSOs (Zheng et al. 2002), while Mrk 231 is an on-going merger with high SFR from its hundred-pc scale molecular disk (Downes & Solomon 1998).

In order to clarify more quantitatively the differences in the spectral properties, we study the properties of  $6.2 \mu\text{m}$  PAH, [NeII]  $12.81 \mu\text{m}$  luminosities, and MIR colour indices  $\alpha(30, 15)$ , for IR QSOs, PG QSOs, and ULIRGs. The infrared colour index is defined as

<sup>2</sup> One exception is 3C 273 for which no scaling was performed since it exhibits large variabilities in the MIR (Neugebauer & Matthews 1999; Hao et al. 2005b).

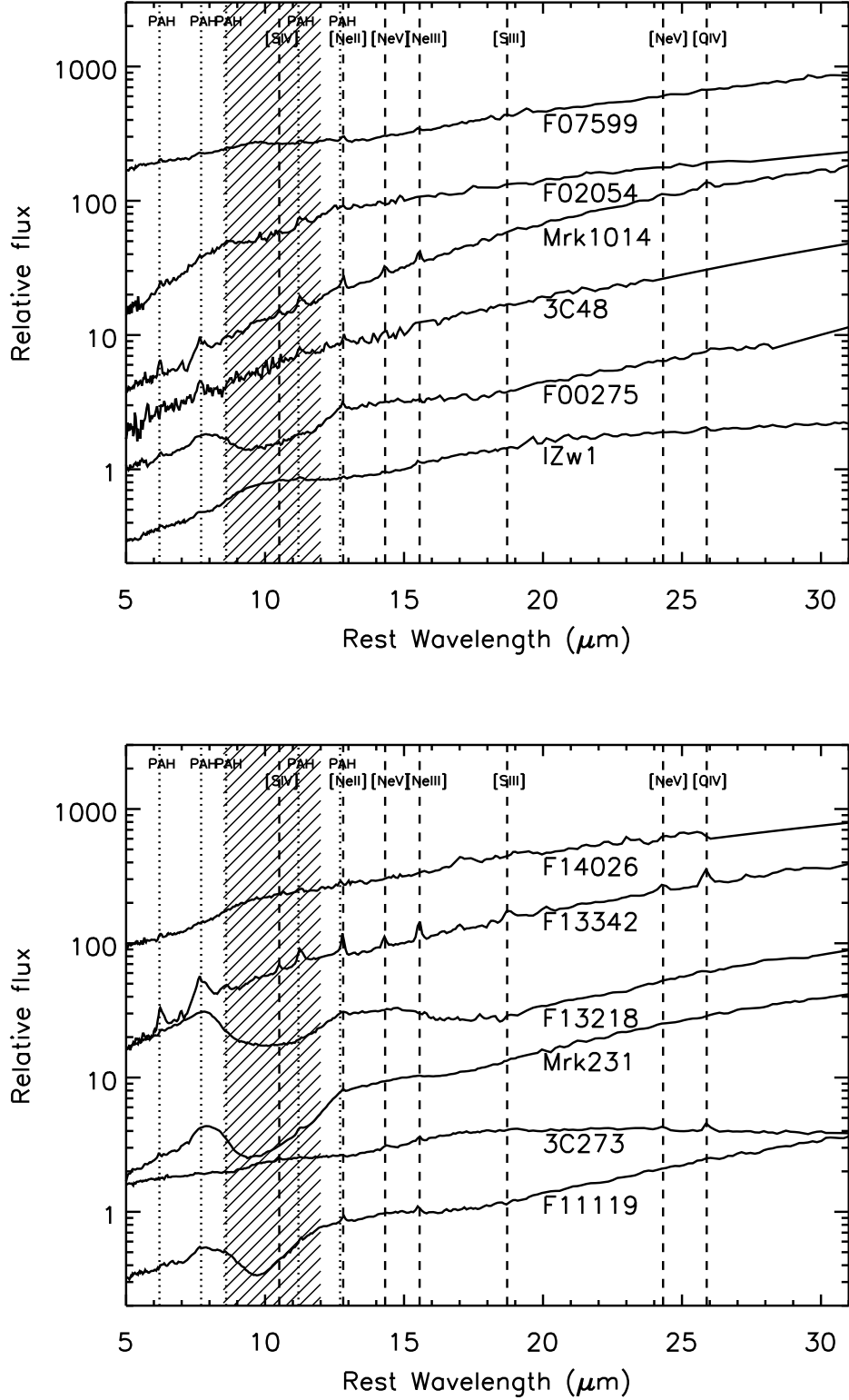


**Figure 1.** Low-resolution *Spitzer*/IRS mid-infrared spectra of 18 IR QSOs in our sample (except for IRAS F21219–1757 which has no LL mode observation), all have been de-redshifted and shifted upward for clarity. The dotted lines show the PAH features at 6.2, 7.7, 8.6, 11.2 & 12.7  $\mu\text{m}$ , and the dashed lines show the mid-infrared fine-structure lines of [SIV]10.51 $\mu\text{m}$ , [NeII]12.81 $\mu\text{m}$ , [NeV]14.32 $\mu\text{m}$ , [NeIII]15.56 $\mu\text{m}$ , [SIII]18.71 $\mu\text{m}$ , [NeV]24.32 $\mu\text{m}$  & [OIV]25.89 $\mu\text{m}$ . The shaded bar denotes the silicate emission/absorption feature centred at 9.7 $\mu\text{m}$ .

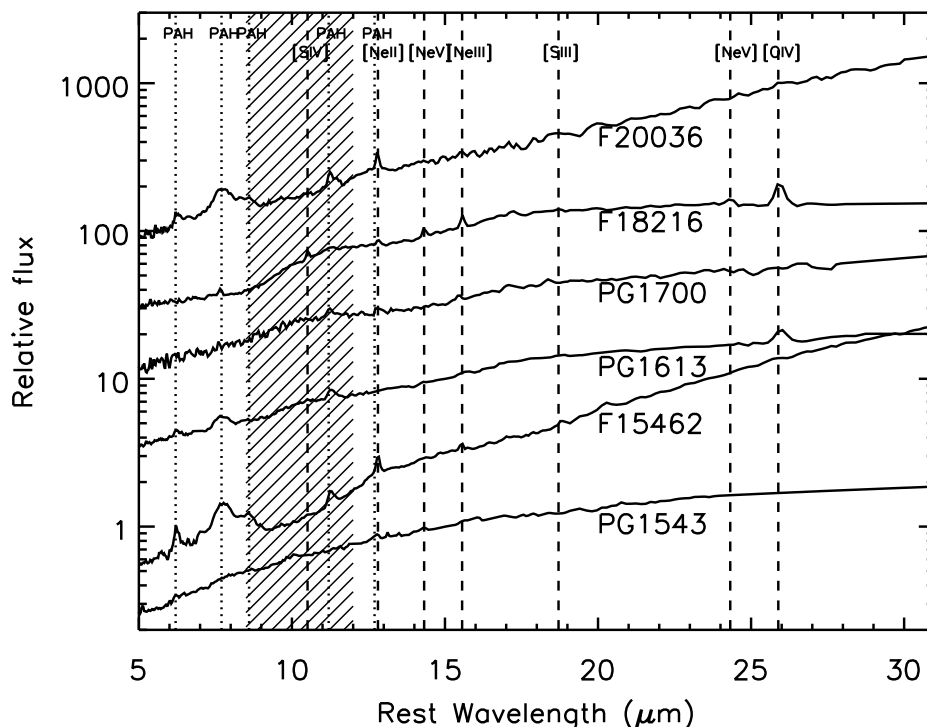


Figure 1. Continued.

$$\alpha(\lambda_1, \lambda_2) = -\frac{\log(F_\nu(\lambda_2)/F_\nu(\lambda_1))}{\log(\lambda_2/\lambda_1)}. \quad (1)$$

The central wavelengths (30 and 15  $\mu\text{m}$ ) are selected in order to avoid the contamination by most strong spectral features (e.g., MIR fine-structure lines, PAH emissions, silicate emission/absorption features etc., see also Brandl et al. 2006; Schweitzer et al. 2006).

The histograms for these quantities are shown in Fig. 3. The mean values of  $\alpha(30, 15)$ , EW (PAH 6.2  $\mu\text{m}$ ), PAH 6.2  $\mu\text{m}$  and [NeII] 12.81  $\mu\text{m}$  luminosities are labelled at the top of each panel of Fig. 3. From the left panels of Fig. 3, the MIR spectral slopes for IR QSOs are much flatter than those of ULIRGs, but are significantly steeper than those of PG QSOs. Since classical QSOs have much lower FIR emissions than IR QSOs at a given bolometric luminosity (Hao et al. 2005a), and  $\alpha(30, 15)$  is correlated with  $\alpha(60, 25)$  (see Fig. 5 and §4.2), it is easy to understand why the  $\alpha(30, 15)$  slopes are steeper for IR QSOs than those of classical QSOs (for details see §4.2). On the other hand, the emissions from hot dust heated by central AGN are mainly in the MIR band. Furthermore, *Spitzer* observations reveal that star formation regions in star-forming galaxies also contribute significantly to the MIR continuum emission (e.g., Wu et al. 2005; Calzetti et al. 2007). Therefore, for IR QSOs, both starburst and central AGN contribute to the MIR continuum emission, leading to the MIR continuum of IR QSOs being stronger than those of ULIRGs. Thus the slopes of MIR to FIR continuum of IR QSOs are flatter than those of ULIRGs.

The histograms of EW (PAH 6.2  $\mu\text{m}$ ) show that

the mean value of EW (PAH 6.2  $\mu\text{m}$ ) of IR QSOs ( $0.031 \pm 0.024 \mu\text{m}$ ) is between those of ULIRGs ( $0.321 \pm 0.235 \mu\text{m}$ ) and PG QSOs ( $0.017 \pm 0.008 \mu\text{m}$ ) and close to that of warm ULIRGs ( $0.04 \pm 0.05 \mu\text{m}$ ; Desai et al. 2007). Considering the fraction of PAH detections for IR QSOs and PG QSOs being 70% (13/19) and 40% (11/27 in QUEST QSO sample) respectively, while the EW (PAH 6.2  $\mu\text{m}$ ) for pure AGN is less than  $0.005\text{--}0.02 \mu\text{m}$  (Armus et al. 2007), the mean value of EW (PAH 6.2  $\mu\text{m}$ ) of IR QSOs is significantly larger than that of classical QSOs.

From the middle and right panels of Fig. 3 we see that the mean values of 6.2  $\mu\text{m}$  PAH and [NeII] 12.81  $\mu\text{m}$  luminosities of IR QSOs are similar to those of ULIRGs, but one order of magnitude higher than those of PG QSOs. Apparently the PAH molecules in IR QSOs can survive the FUV and X-ray photons emitted by central AGN, suggesting that they are shielded by a large amount of gas and dust from radiation (see Schweitzer et al. 2006).

Since the bolometric luminosities ( $L_{\text{bol}}$ ) of PG QSOs observed by IRS of *Spitzer* are systematically smaller than those of IR QSOs, where  $L_{\text{bol}}$  is calculated from the optical continuum emission ( $L_{\text{bol}} \approx 9\lambda L_\lambda(5100\text{\AA})$ , Hao et al. 2005a), the differences in their IR continuum shapes may simply arise because more optically luminous QSOs have more extended dust tori. To check this possibility, we investigated the 6.2  $\mu\text{m}$  PAH and [NeII] 12.81  $\mu\text{m}$  luminosities normalised by  $L_{\text{bol}}$ . Fig. 4 shows the distributions of  $L_{\text{PAH}}/L_{\text{bol}}$  and  $L_{\text{[NeII]}}/L_{\text{bol}}$  for IR QSOs and PG QSOs, respectively. It is clear from Fig. 4 that the mean values of  $L_{\text{PAH}}/L_{\text{bol}}$  and  $L_{\text{[NeII]}}/L_{\text{bol}}$  for IR QSOs are also about one order of mag-

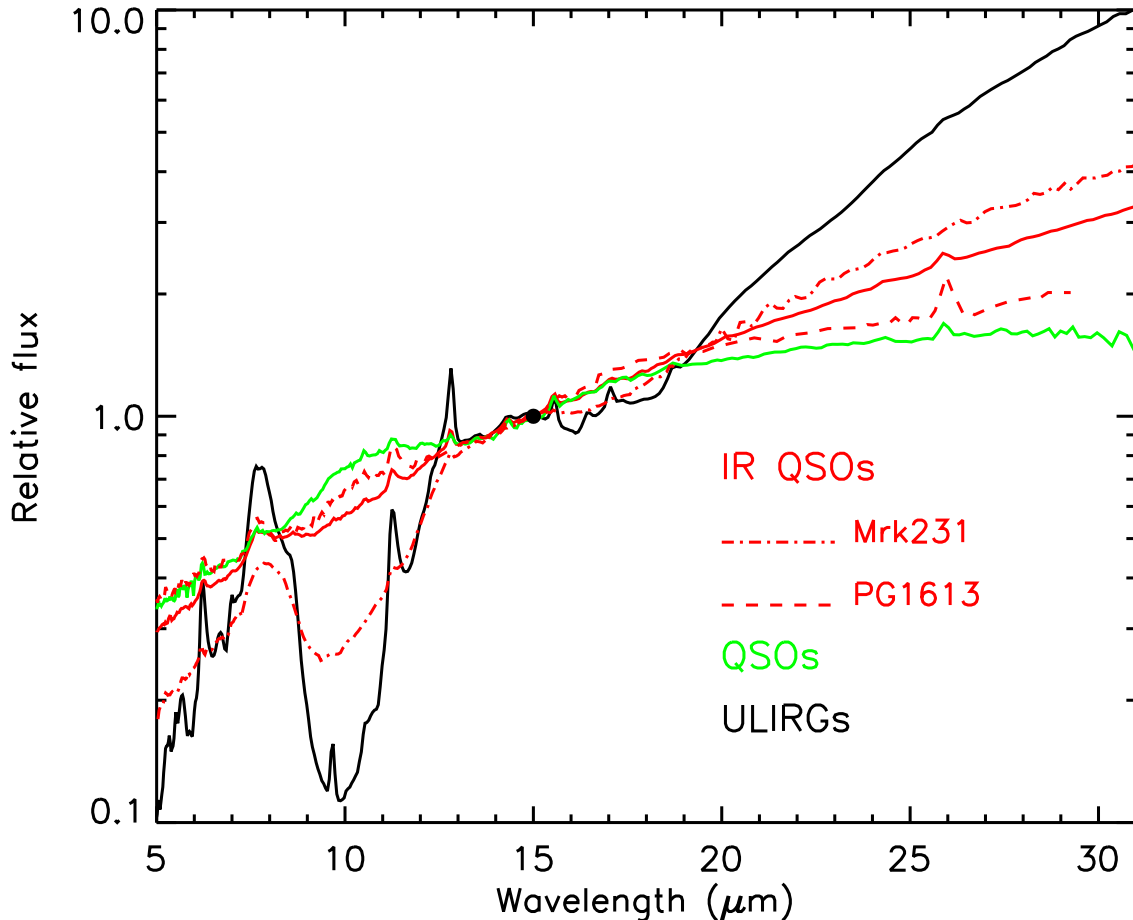


**Figure 2.** Average MIR IRS low-resolution spectra of IR QSOs (red solid line) in our sample, and QSOs (green), ULIRGs (black) from Hao et al. (2007), normalised to  $f(15\mu\text{m})=1$  (denoted by a black dot). Spectra of two representative IR QSOs (PG 1613+658 and Mrk 231) are also shown by red dashed and red dot-dashed lines.

nitude higher than those of PG QSOs. Therefore, the different properties of  $6.2\mu\text{m}$  PAH and  $[\text{NeII}]12.81\mu$  emissions between IR QSOs and PG QSOs are unlikely from different dust tori, instead the differences arise because of different star formation properties (see section 4.2).

In summary, the mid-IR spectroscopic properties, including the continuum slope and emission line strengths, of IR QSOs, PG QSOs and ULIRGs are consistent with that IR QSOs are in a transitional phase from ULIRGs to classical QSOs, confirming the results from previous studies (Canalizo & Stockton 2001; Hao et al. 2005a).

#### 4.2 Statistics on spectral parameters

In this subsection, we will use the MIR spectroscopic features, including the MIR continuum slope  $\alpha(30, 15)$ ,  $6.2\mu\text{m}$  PAH and fine-structure emission lines, to investigate the origin of MIR emissions of IR QSOs. We will also use these properties, combined with FIR and optical properties, to disentangle the starburst and AGN contributions in these objects.

Fig. 5 shows the relations of  $\alpha(30, 15)$  vs.  $\alpha(60, 25)$

(left panel),  $\alpha(30, 15)$  vs. the FIR excess  $L_{60\mu\text{m}}/L_{\text{bol}}$  (middle panel), and  $\alpha(30, 15)$  vs. the EW (PAH  $6.2\mu\text{m}$ ) (right panel) for both IR QSOs and PG QSOs. It is clear from Fig. 5 that the colour indices of  $\alpha(30, 15)$  and  $\alpha(60, 25)$  are closely correlated, indicating that  $\alpha(30, 15)$  can express the relative strength of FIR to MIR emission for QSOs. The middle and right panels of Fig. 5 show the correlations between  $\alpha(30, 15)$  with FIR excess  $L_{60\mu\text{m}}/L_{\text{bol}}$ , and between  $\alpha(30, 15)$  with the EW (PAH  $6.2\mu\text{m}$ ). The EW (PAH  $6.2\mu\text{m}$ ) is the ratio of PAH  $6.2\mu\text{m}$  emission line to  $\sim 6\mu\text{m}$  continuum. Since the  $6.2\mu\text{m}$  PAH emission is from star formation regions, and the  $6\mu\text{m}$  continuum traces the AGN contribution (e.g., Gallagher et al. 2007), thus the EW (PAH  $6.2\mu\text{m}$ ) expresses the relative contribution of star formation to AGN (Schweitzer et al. 2006; Armus et al. 2007). In fact, Desai et al. (2007) also found the strong correlation between infrared spectral slope and the EW (PAH  $6.2\mu\text{m}$ ) for ULIRGs, especially for ULIRGs with Seyfert 1 and Seyfert 2 optical spectra, while our results extend such relation to infrared luminous QSOs and PAH detected PG QSOs. We conclude that  $\alpha(30, 15)$ , FIR excess and EW (PAH  $6.2\mu\text{m}$ )

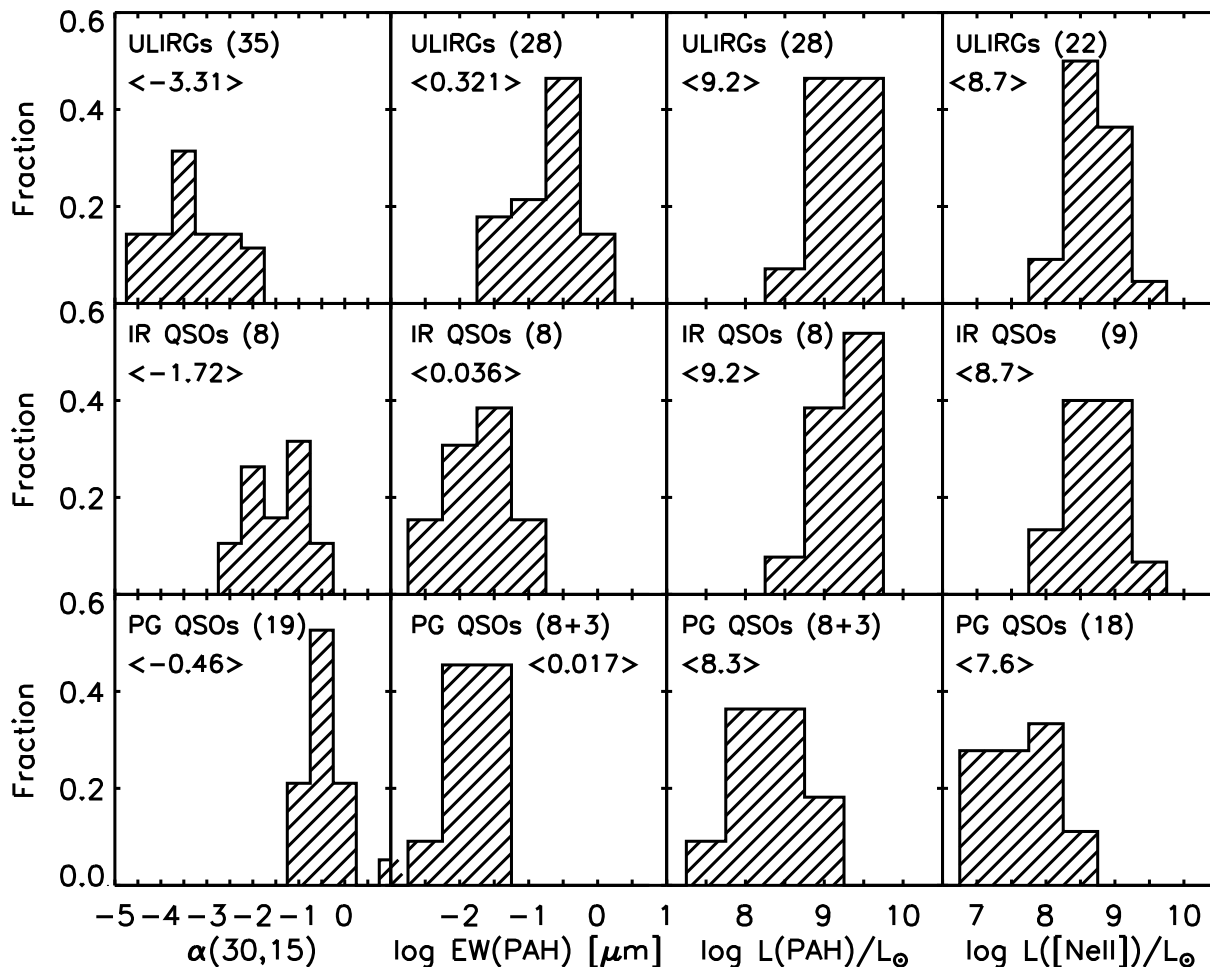


**Figure 3.** From left to right: histograms of MIR colour index  $\alpha(30, 15)$ , the EW (PAH  $6.2\mu\text{m}$ ), the  $6.2\mu\text{m}$  PAH and  $12.8\mu\text{m}$  [NeII] line luminosities for ULIRGs (top), IR QSOs (middle), and PG QSOs (bottom) with detectable PAH and [NeII] emissions. The mean values are labelled in the panels, and the number of objects used in each histogram is in the bracket. Notice that the histogram of  $L(\text{[NeII]})$  for PG QSOs is from the sample by Schweitzer et al. (2006), while the [NeII] luminosities for ULIRGs are derived from Farrah et al. (2007b).

can serve as indicators of the relative contributions of starbursts to AGNs (Hao et al. 2005a and see below).

Ho & Keto (2007) suggest that the ionised neon fine-structure lines [NeII] $12.81\mu\text{m}$  and [NeIII] $15.56\mu\text{m}$  can be used as a SFR indicator for star-forming galaxies. Farrah et al. (2007b) extend this relation to ULIRGs. In addition, Schweitzer et al. (2006) found a strong correlation between the far-infrared continuum ( $L_{60\mu\text{m}}$ ) and low-ionisation [NeII] line emission for both PG QSOs and ULIRGs, and argued that the [NeII] line can also be used to estimate the SFR in QSO host galaxies. One advantage to use [NeII]  $12.81\mu\text{m}$  as a SFR estimator is that it suffers much less extinction than optical lines, such as  $H\alpha$  and [OII] $3727\text{\AA}$ . However, there is still a debate about the origin of [NeII] emission, because the narrow line region of QSOs may also contribute substantially (e.g., Ho & Keto 2007). Therefore, it is worth investigating the origin of [NeII] $12.81\mu\text{m}$  emission for IR QSOs by comparing the multi-wavelength properties of PG QSOs, IR QSOs and ULIRGs.

Fig. 6 shows the relation between PAH  $6.2\mu\text{m}$  and [NeII] $12.81\mu\text{m}$  luminosities for IR QSOs, ULIRGs and PG QSOs with firmly detected [NeII] $12.81\mu\text{m}$  and PAH  $6.2\mu\text{m}$  emissions. Because the PAH emissions are purely from star formation regions (Shi et al. 2007), the tight correlation between  $6.2\mu\text{m}$  PAH and [NeII] $12.81\mu\text{m}$  luminosities (at a statistical level of  $> 99.99\%$  with the Spearman Rank-order test) demonstrates that (at least part of) the [NeII] $12.81\mu\text{m}$  emission is also from star formation regions. Note that for the PG QSOs shown in Fig. 6, their [NeII]  $12.81\mu\text{m}$  luminosities normalised by the bolometric luminosities of AGNs ( $L_{[\text{NeII}]} / L_{\text{bol}}$  ratios, see below) are about three times higher than that of PAH undetected PG QSOs (see also Schweitzer et al. 2006). Therefore, it is likely that the star formation contributes significantly to the [NeII] emission not only for IR QSOs, but also for PG QSOs with detectable PAH emissions (Netzer et al. 2007).

The mean values of  $L_{[\text{NeII}]} / L_{\text{bol}}$  ratios are  $3.4 \pm 3.5 \times 10^{-4}$ ,  $5.3 \pm 3.6 \times 10^{-5}$ ,  $8.1 \pm 5.2 \times 10^{-5}$  and  $2.7 \pm 1.4 \times 10^{-5}$  for IR QSOs, PG QSOs, PAH-detected and PAH-undetected

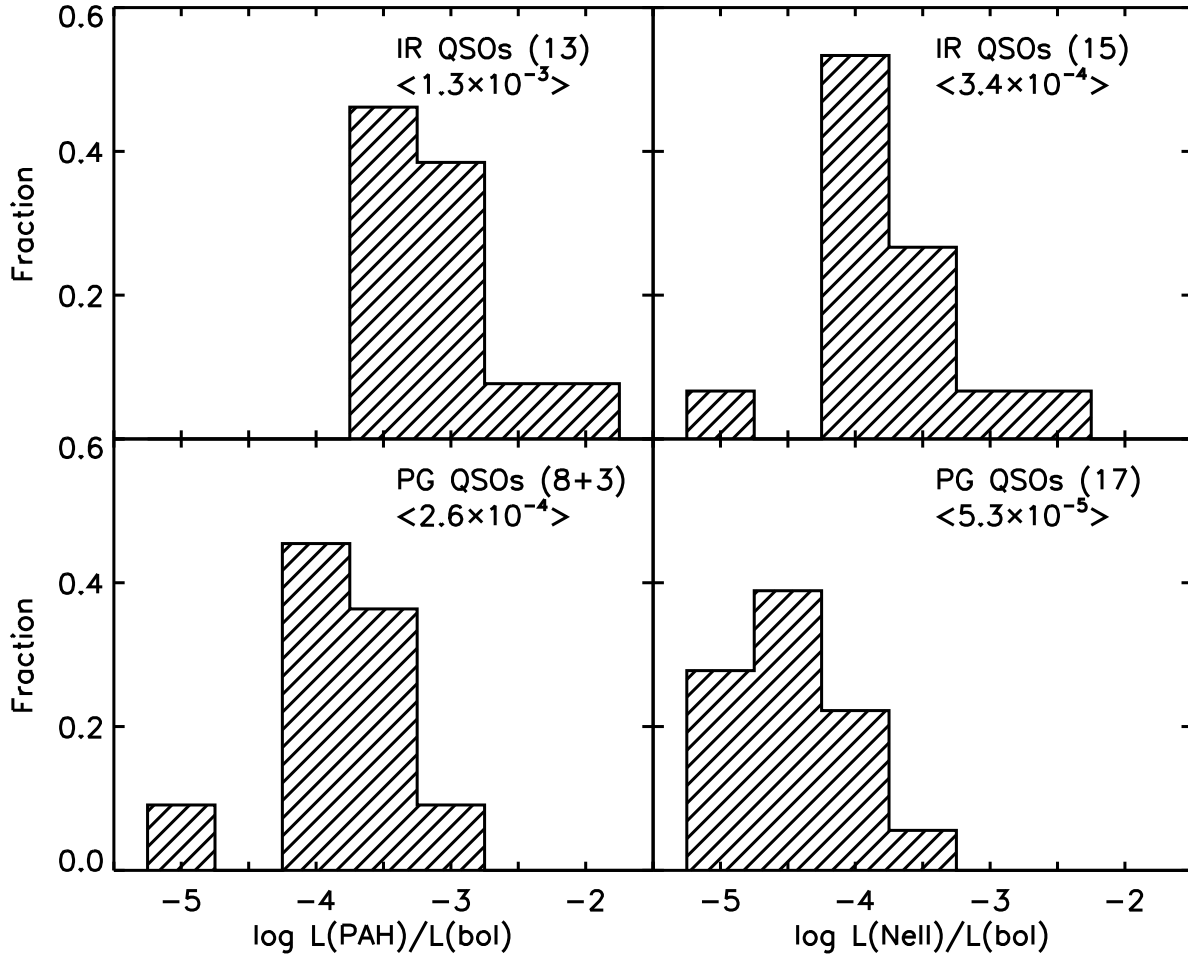


**Figure 4.** Histograms of the  $6.2\mu\text{m}$  PAH (left) and  $12.8\mu\text{m}$  [NeII] line (right) luminosities normalised by the bolometric luminosity for IR QSOs (top) and PG QSOs (bottom) with detectable PAH and [NeII] emissions. The mean values are labelled in the panels, and the number of objects used in each histogram is in the bracket. Notice that the histogram of  $L_{\text{[NeII]}}/L_{\text{bol}}$  for PG QSOs is from the sample of Schweitzer et al. (2006).

PG QSOs, respectively. Thus for the same bolometric luminosity of a central AGN, the mean [NeII] $12.81\mu\text{m}$  luminosity of IR QSOs is about one order of magnitude higher than that of classical QSOs. Taken together with the tight correlation between [NeII] and PAH luminosities (see above), we conclude that the [NeII] $12.81\mu\text{m}$  emission of IR QSOs is mainly from star formation, while the contribution from the narrow line region of AGNs is not significant ( $\lesssim 10\%$ ).

## 5 DISCUSSION

By comparing the MIR spectroscopic properties of IR QSOs, ULIRGs and PG QSOs, we found that the indicators of relative contributions of starbursts to AGNs (such as colour index  $\alpha(30, 15)$  and EW [PAH  $6.2\mu\text{m}$ ]) for IR QSOs are between those of ULIRGs and PG QSOs. These results are consistent with the findings of Canalizo & Stockton (2001) and Hao et al. (2005a) that (at least some) infrared luminous QSOs (IR QSOs) are at a transitional stage from ULIRGs to

classical QSOs. Below we consider the star formation rates and AGN/star formation feedback in more detail.

### 5.1 SFR determined by the [NeII] $12.81\mu\text{m}$ and PAH luminosities

As we argued, the AGN contribution to [NeII] emission for ULIRGs and IR QSOs is probably very small, and there is a tight correlation between [NeII] $12.81\mu\text{m}$  and PAH  $6.2\mu\text{m}$  luminosities (see §4.2). We examine in more detail how they can be used as approximate SFR indicators for ULIRGs and IR QSOs.

Fig. 7 shows the [NeII] $12.81\mu\text{m}$  (top panel) and PAH  $6.2\mu\text{m}$  (bottom panel) luminosities versus the  $60\mu\text{m}$  luminosity for IR QSOs, PG QSOs and ULIRGs with firmly detected [NeII] $12.81\mu\text{m}$  and PAH  $6.2\mu\text{m}$  emissions. A Spearman Rank-order analysis show that both correlations are significant at  $> 99.99\%$  level. The dashed lines in Fig. 7 represent the least-squares regression fits:

$$\log L_{\text{NeII}} = (0.90 \pm 0.06) \log L_{60\mu\text{m}} - (2.22 \pm 0.69), \quad (2)$$



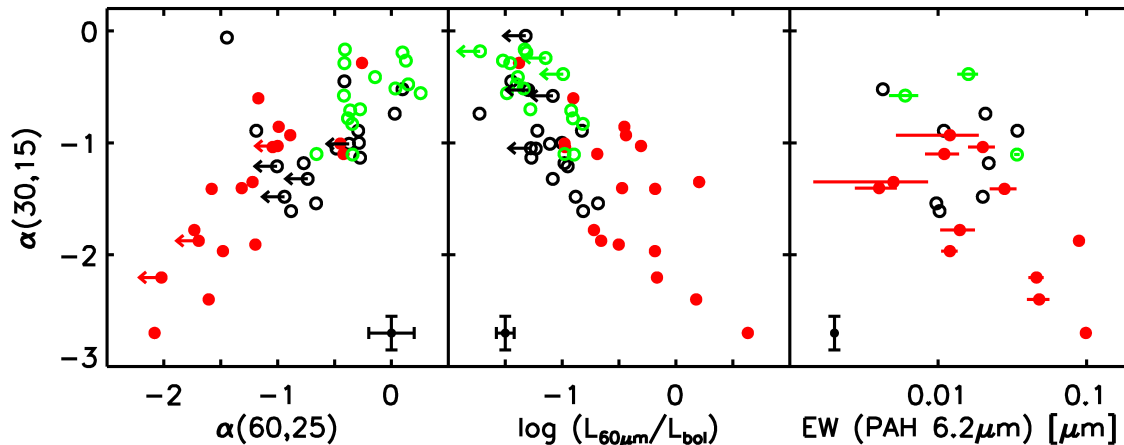


**Figure 5.** From left to right: MIR colour index  $\alpha(30, 15)$  vs. infrared colour index  $\alpha(60, 25)$ ; vs. infrared excess ( $L_{60\mu\text{m}}/L_{\text{bol}}$ ); vs. EW (PAH  $6.2\mu\text{m}$ ) for IR QSOs (red filled circle) and PG QSOs (green and black open circle for PG QSOs from our sample and Schweitzer et al. 2006). The horizontal and/or vertical bars on the bottom right of each panel indicate the mean errors on the  $\alpha(60, 25)$ ,  $L_{60\mu\text{m}}/L_{\text{bol}}$ , and  $\alpha(30, 15)$  values.

$$\log L_{\text{PAH}} = (0.78 \pm 0.06) \log L_{60\mu\text{m}} - (0.31 \pm 0.74). \quad (3)$$

The fitting formula (2) is consistent with that of Ho & Keto (2007) for star-forming galaxies (within the large errors). Note that our sample objects have much higher  $60\mu\text{m}$  and [NeII]  $12.81\mu\text{m}$  and PAH  $6.2\mu\text{m}$  luminosities than their star-forming galaxies. Thus both [NeII]  $12.81\mu\text{m}$  and PAH  $6.2\mu\text{m}$  luminosities can be used as approximate SFR indicators not only for normal star-forming galaxies, but also for galaxies with high infrared luminosities, such as ULIRGs and IR QSOs (see Brandl et al. 2006 and Farrah et al. 2007b).

However, the mean scatters (about 0.7 to 0.8 dex) in the relation of [NeII]  $12.81\mu\text{m}$ , PAH  $6.2\mu\text{m}$  with  $60\mu\text{m}$  luminosities are larger than that (about 0.6 dex) of star-forming galaxies with lower infrared luminosity (Ho & Keto 2007). Comparing Fig. 7 with Fig. 6, one can see that the scatter in the relation of [NeII]  $12.81\mu\text{m}$  vs. PAH  $6.2\mu\text{m}$  luminosities (about 0.6 dex) is smaller than that in the relations of [NeII]  $12.81\mu\text{m}$ , PAH  $6.2\mu\text{m}$  luminosities with  $L(60\mu\text{m})$ . It is also clear that most large scatters are from ULIRGs. This is perhaps not surprising since the range in the  $9.7\mu\text{m}$  silicate absorption depth among ULIRGs is quite large (see Armus et al. 2007, Spoon et al. 2007). In short, the large scatters for ULIRGs seen in the relations may be due to complicated, patchy extinctions among these galaxies in the MIR band. A detailed discussion on extinction for ULIRGs can be found in Farrah et al. (2007b).

## 5.2 AGN/Star formation feedback in the transitional stage

One explanation for the observed correlation between spheroidal and black hole mass (e.g., Magorrian et al. 1998; Ferrarese & Ford 2005) is that star formation and the growth of central black holes may be self-regulated: AGNs/star formation can drive nuclear outflows which in turn suppress further cooling and star formation (Silk & Rees 1998). While the detailed processes are still

to be understood, it is now increasingly clear that feedback and outflows play an important role in galaxy formation and evolution.

So far most observational evidence for AGN feedback is from radio observations at the centre of clusters or groups of galaxies (Batcheldor et al. 2007). On the galaxy scale, evidence is still limited. As discussed above, IR QSOs have high SFRs and accretion rates (Hao et al. 2005a), outflow properties in these objects may thus provide hints on the feedback processes on galaxy or group scale.

It is well known that low-ionisation broad absorption line QSOs (loBAL QSOs) comprise about 15% of BAL QSO population. They are defined as a subclass of BAL QSOs with an obvious blueshifted absorption in Mg II  $\lambda\lambda 2795, 2802$  and other low-ionisation species (Weymann et al. 1991). Such absorption troughs arise from resonance absorption by outflowing gas and dust (Voit et al. 1993). In addition, there is a rare class of loBAL QSOs, showing absorption features from excited iron (termed as FeLoBAL QSOs). The outflow velocities for most BAL QSOs span a large range, up to a few times  $10^4 \text{ km s}^{-1}$ , which may be formed on a scale of  $< 1 \text{ pc}$  and directly associated with the wind from an accretion disk or molecular torus (Weymann et al. 1985). However, recent spectral analyses based on Keck observations for LoBAL QSOs or FeLoBAL QSOs reveal that the outflow velocities of some LoBAL QSOs range from several hundred to several thousand  $\text{km s}^{-1}$  and the wind is from regions of a few hundred pc (e.g., Ganguly & Brotherton 2008; Hamann et al. 2000; de Kool et al. 2002), which is much larger than the central engine of AGNs, but similar to the size of the nuclear starburst region of ULIRGs (Downes & Solomon 1998).

On the other hand, Canalizo & Stockton (2002) studied four loBAL QSOs at  $z < 0.4$  (Mrk 231, IRAS 14026+4341, IRAS F07599+6508, PG 1700+518; all four are in our sample) and found that all are ULIRGs with merging signatures. They argued that loBAL QSOs cannot simply be explained by orientation effects, rather, they are directly re-

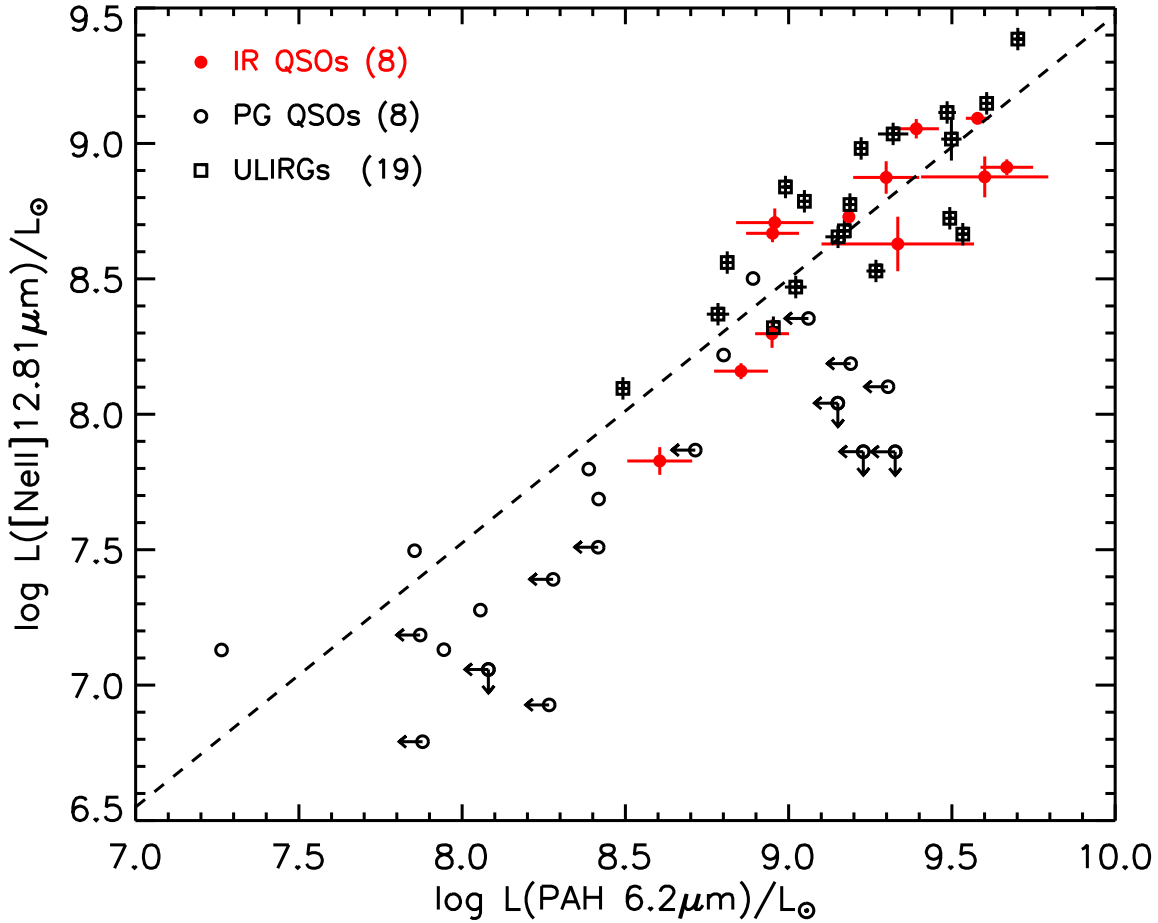


**Figure 6.** The PAH 6.2  $\mu\text{m}$  vs. [NeII] 12.81  $\mu\text{m}$  luminosities for IR QSOs, PG QSOs (from Schweitzer et al. 2006), and ULIRGs in our sample which have [NeII] measurements by Farrah et al. (2007b). The number of each type of galaxies is indicated in the bracket, while the dashed line represents the linear regression for all sample objects. Note we excluded objects with undetected (upper-limits) PAH or [NeII] emissions in the regression analysis. The Spearman Rank-order (S-R) correlation analysis gives the coefficient of linear regression as 0.89 with significance of  $> 99.99\%$  for the above correlation.

lated to young systems, still surrounded by gas and dust. It represents a short stage in the early life of a large fraction of QSOs. Moreover, Farrah et al. (2007a) reported the detections of mid/far-infrared emission from 9 FeLoBAL QSOs by MIPS. They found that all of their objects are IR bright with infrared luminosities as high as ULIRGs. Thus all loBAL QSOs and FeLoBAL QSOs with MIR to FIR information are infrared ultra-luminous, suggesting a link among loBAL QSOs, FeLoBAL QSOs and IR QSOs.

For loBAL QSOs or FeLoBAL QSOs, the velocities of outflows can be measured from blueshifted absorption lines. Unfortunately it is still unclear whether most IR QSOs are loBAL QSOs or FeLoBAL QSOs, because not many IR QSOs have been observed in the UV. However, there are measurements for the blueshifts in the permitted optical emission lines for our IR QSO sample (Zheng et al. 2002). The line profiles often contain two Gaussian components, one broad and one narrow. The outflow velocities are determined by the blueshift of the broad Gaussian component relative to the narrow component of permitted emission lines

(H $\beta$ ) for IR QSOs (see Zheng et al. 2002). We assume the blueshifted broad Gaussian component is related to the outflow of clouds (Leighly 2001; Batcheldor et al. 2007).

Fig. 8 shows the correlation between EW (PAH 6.2  $\mu\text{m}$ ) and outflow velocities for IR QSOs. As the outflow velocity increases, the EW (PAH 6.2  $\mu\text{m}$ ) decreases. Since the EW (PAH 6.2  $\mu\text{m}$ ) expresses the relative contribution of star formation to AGN in QSOs (see §4.2), the correlation shown in Fig. 8 implies that QSOs with higher outflow velocities have a lower ratio of SFR to accretion rate. It may be because more energetic AGNs and central massive starbursts can drive faster outflows which then suppress or even quench star formation by heating up or expelling the cold gas and dust in the QSO hosts, leading to a lower ratio of SFR to accretion rate. Another possibility is that the higher velocity outflows are more efficient in ejecting dust cocoons of AGNs, leading to AGNs becoming the dominant source compared with starbursts. We should caution, however, that the sample shown in Fig. 8 is small; a larger sample would allow us to

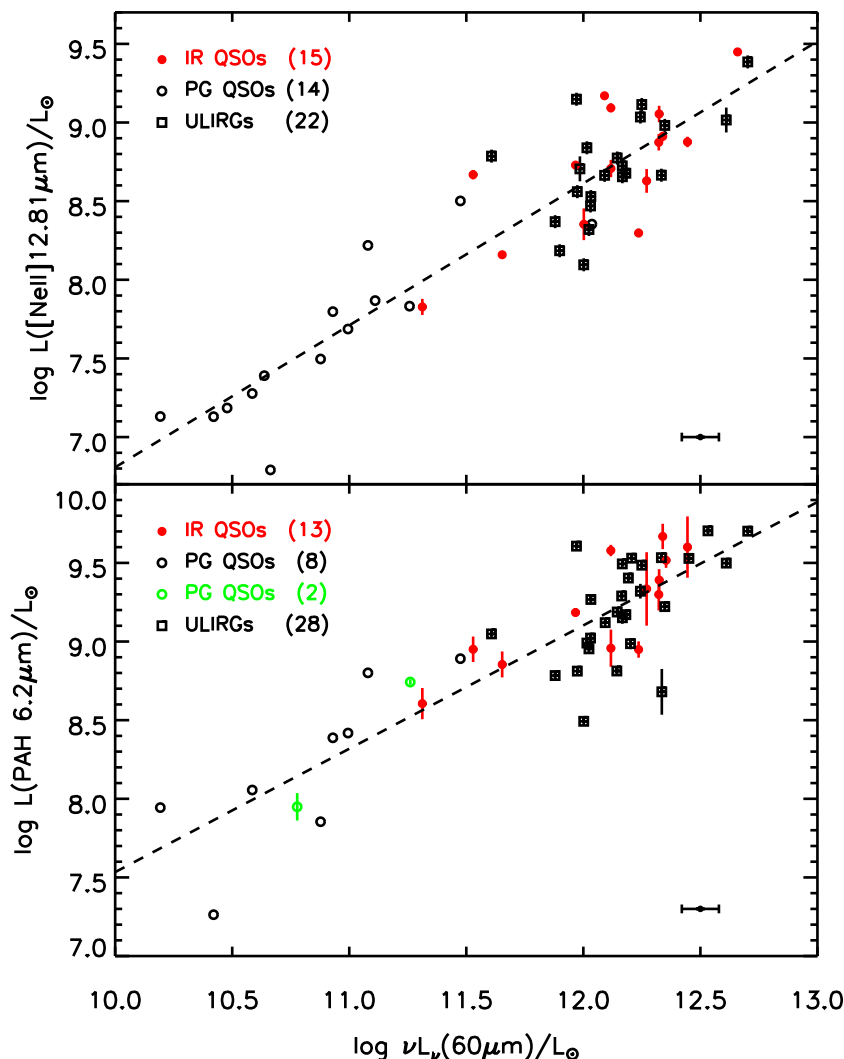


**Figure 7.** Top panel: Luminosities  $L(60\mu\text{m})$  vs.  $L([\text{NeII}]12.81\mu\text{m})$  for IR QSOs, PG QSOs (from Schweitzer et al. 2006), and ULIRGs with detectable  $[\text{NeII}]$  and  $60\mu\text{m}$  emissions. Bottom panel: Luminosities  $L(60\mu\text{m})$  vs.  $L(\text{PAH } 6.2\mu\text{m})$  for IR QSOs, PG QSOs in our sample (green) and from Schweitzer et al. (2006) (black), and ULIRGs with detectable PAH and  $60\mu\text{m}$  emissions. The  $6.2\mu\text{m}$  PAH fluxes for PG QSOs from Schweitzer et al. (2006) were estimated by assuming a  $7.7/6.2$  flux ratio of 4.7 derived from the measurement of the ULIRG NGC 6240 with a buried AGN (Armus et al. 2006). The number of each galaxy type is indicated in the bracket, while the dashed lines represent the linear regressions for the above two correlations. The horizontal bar on the bottom right of each panel indicates the mean error of the  $60\mu\text{m}$  luminosity.

better understand the relative importance of star formation and AGN in feedback and driving outflows.

## 6 SUMMARY

In this work, we studied the MIR spectral properties of low-redshift IR QSOs based on spectroscopic observations with *Spitzer* IRS, and compared their properties with those of ULIRGs and optically-selected PG QSOs. The following are our main results:

1. The average MIR spectra, MIR spectral slopes,  $6.2\mu\text{m}$  PAH emission strengths and  $[\text{NeII}]$   $12.81\mu\text{m}$  luminosities of IR QSOs are distinct from those of PG QSOs. The MIR properties of IR QSOs are intermediate between ULIRGs

and optically-selected QSOs, indicating that IR QSOs are at a transitional stage from ULIRGs to classical QSOs.

2. From the correlations between  $\alpha(30, 15)$  with  $\alpha(60, 25)$ , FIR excess  $L_{60\mu\text{m}}/L_{\text{bol}}$ , and EW (PAH  $6.2\mu\text{m}$ ) for both IR QSOs and PG QSOs, we find that the MIR colour index  $\alpha(30, 15)$  is a good indicator of the relative contribution of starbursts to AGNs for all QSOs.

3. Both PAH and  $[\text{NeII}]12.81\mu\text{m}$  luminosities of IR QSOs are in the same range as those of ULIRGs, but are one order of magnitude higher than those of PG QSOs (see Fig. 3). From the tight correlation between PAH  $6.2\mu\text{m}$  and  $[\text{NeII}]$   $12.81\mu\text{m}$  luminosities for IR QSOs, ULIRGs and PAH detected PG QSOs, and the fact that the  $L_{[\text{NeII}]} / L_{\text{bol}}$  ratio for IR QSOs is about one order of magnitude higher than that of classical QSOs, we conclude that the  $[\text{NeII}]$   $12.81\mu\text{m}$

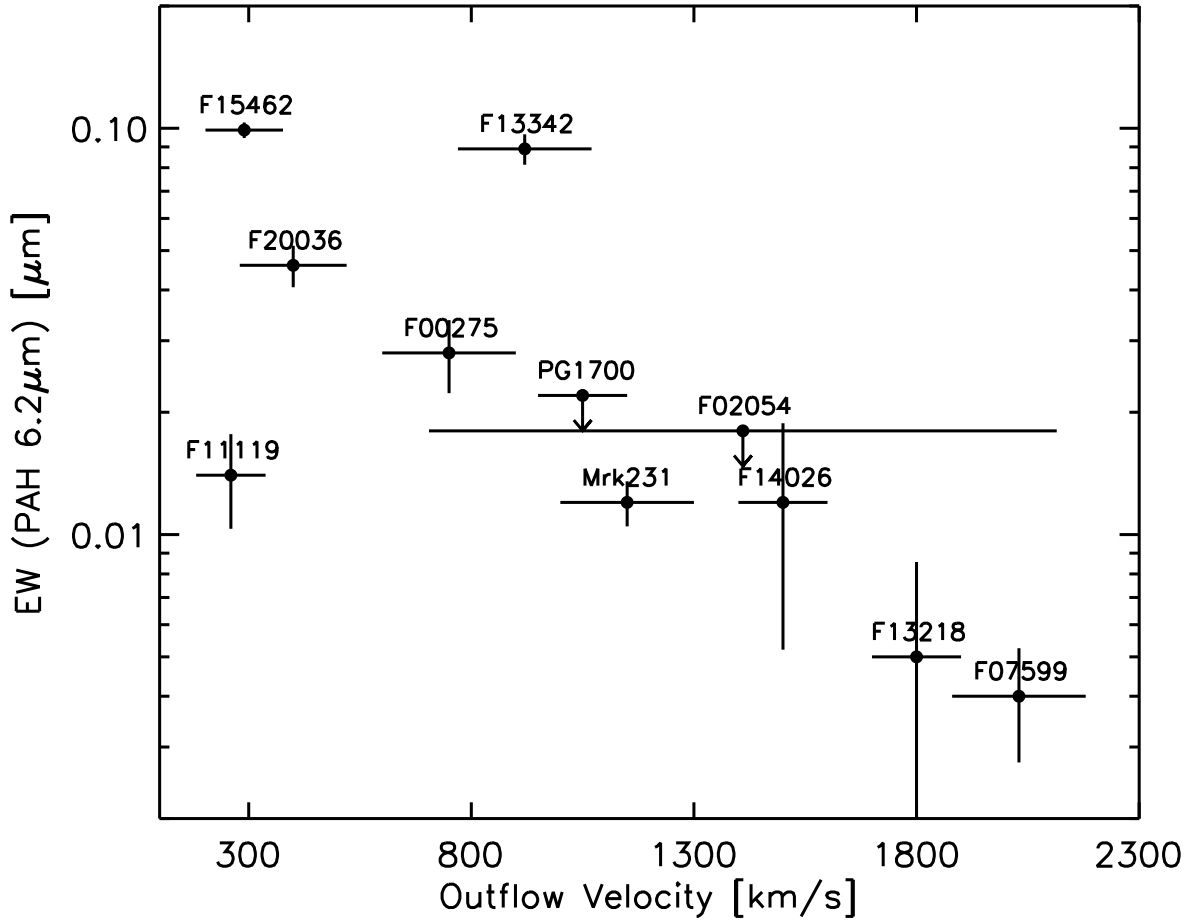


**Figure 8.** The velocity of outflows vs. the equivalent width of the  $6.2\mu\text{m}$  PAH emission feature ( $\text{EW}(\text{PAH } 6.2\mu\text{m})$ ) for eleven IR QSOs (black filled circle) which show obvious  $\text{H}\beta$  blueshifts. The Kendalls ( $\tau$ ) rank correlation analysis gives coefficient of linear regression as  $-0.66$  with a significance of 99.5%. The outflow velocities were derived from the  $\text{H}\beta$  emission line profiles (Zheng et al. 2002; Lípari et al. 2005).

emission of IR QSOs is dominated by star formation, thus their luminosity can be used as an approximate indicator of their SFRs.

4. Outflows in IR QSOs play an important role in suppressing star formation by heating and/or expelling cold gas surrounding nuclei of QSOs. Thus IR QSOs are an important observational sample to investigate AGN and star formation feedback processes.

## ACKNOWLEDGEMENTS

We thank the anonymous referee for constructive comments and suggestions. We acknowledge Drs. J. Wang, D.-W. Xu, Y. Shi, S. Veilleux for advice and helpful discussions. We also thank Z.-H. Shang, Y.-L. Wu, K. Zhang for helpful discussion on the *Spitzer* IRS data reductions, and Sarah Bryan for a careful reading of the manuscript. CC acknowledges the support of the Tianjin Astrophysics Center (TAC) at Tianjin Normal University, and the full living and travel supports of the European Union Marie Curie Program for

him to participate in the AGN/VLTI summer school held in Poland, 2007. SM acknowledges the travel support of the NSFC, the Chinese Academy of Sciences and the Tianjin municipal government. This work is based on observations made with the *Spitzer Space Telescope*, which is operated by the Jet Propulsion Laboratory, California Institute of Technology under a contract with NASA. The IRS was a collaborative venture between Cornell University and Ball Aerospace Corporation funded by NASA through the Jet Propulsion Laboratory and Ames Research Center. SMART was developed by the IRS Team at Cornell University and is available through the Spitzer Science Center at Caltech. This research has made use of the NASA/IPAC Extragalactic Database (NED) which is operated by the Jet Propulsion Laboratory, California Institute of Technology, under contract with the National Aeronautics and Space Administration. This project is supported by the NSF of China 10333060, 10778622 and 973 Program No.2007CB815405, 2007CB815406.

## REFERENCES

- Armus L., et al., 2006, ApJ, 640, 204
- Armus L., et al., 2007, ApJ, 656, 148
- Batcheldor D., Tadhunter C., Holt J., Morganti R., O'Dea C. P., Axon D. J., & Koekemoer A., 2007, ApJ, 661, 70
- Boroson T. A., & Green R. F., 1992, ApJS, 80, 109
- Brandl B. R., et al., 2006, ApJ, 653, 1129
- Calzetti D., et al., 2007, ApJ, 666, 870
- Canalizo G., & Stockton A., 2001, ApJ, 555, 719
- Canalizo G., & Stockton A., 2002, ASP Conf. Ser. 255: Mass Outflow in Active Galactic Nuclei: New Perspectives, 255, 195
- Carilli C. L., et al., 2007, ApJS, 172, 518
- Cui J., Xia X.-Y., Deng Z.-G., Mao S., & Zou Z.-L., 2001, AJ, 122, 63
- Desai V., et al., 2007, ApJ, 669, 810
- Downes D., & Solomon P. M., 1998, ApJ, 507, 615
- de Kool M., Becker R. H., Arav N., Gregg M. D., & White R. L., 2002, ApJ, 570, 514
- Evans A. S., Solomon P. M., Tacconi L. J., Vavilkin T., & Downes D., 2006, AJ, 132, 2398
- Farrah D., Lacy M., Priddey R., Borys C., & Afonso J., 2007a, ApJ, 662, L59
- Farrah D., et al., 2007b, ApJ, 667, 149
- Ferrarese L., & Ford H., 2005, Space Science Reviews, 116, 523
- Gallagher S. C., Richards G. T., Lacy M., Hines D. C., Elitzur M., & Storrie-Lombardi L. J., 2007, ApJ, 661, 30
- Ganguly R., & Brotherton M. S., 2008, ApJ, 672, 102
- Haas M., et al., 2003, A&A, 402, 87
- Hamann F. W., Netzer H., & Shields J. C., 2000, ApJ, 536, 101
- Hao C. N., Xia X. Y., Mao S., Wu H., & Deng Z. G., 2005a, ApJ, 625, 78
- Hao C. N., Xia X. Y., Mao S., Deng Z. G., & Wu H., 2008, Chinese Journal of Astronomy and Astrophysics, 8, 12
- Hao L., et al., 2005b, ApJ, 625, L75
- Hao L., Weedman D. W., Spoon H. W. W., Marshall J. A., Levenson N. A., Elitzur M., & Houck J. R., 2007, ApJ, 655, L77
- Heckman T. M., Kauffmann G., Brinchmann J., Charlot S., Tremonti C., & White S. D. M., 2004, ApJ, 613, 109
- Higdon S. J. U., et al., 2004, PASP, 116, 975
- Ho L. C., 2005, ApJ, 629, 680
- Ho L. C., & Keto E., 2007, ApJ, 658, 314
- Houck J. R., Schneider D. P., Danielson, G. E., Neugebauer, G., Soifer B. T., Beichman, C. A., & Lonsdale, C. J. 1985, ApJ, 290, L5
- Houck J. R., et al., 2004, ApJS, 154, 18
- Imanishi M., Dudley C. C., Maiolino R., Maloney P. R., Nakagawa T., & Risaliti G., 2007, ApJS, 171, 72
- Kim D.-C., & Sanders D. B., 1998, ApJS, 119, 41
- Lawrence, A., et al. 1999, MNRAS, 308, 897
- Leighly K. M., 2001, Probing the Physics of Active Galactic Nuclei, 224, 293
- Lípari S., Terlevich R., Zheng W., Garcia-Lorenzo B., Sanchez S. F., & Bergmann M., 2005, MNRAS, 360, 416
- Lonsdale C. J., Farrah D., & Smith H. E., 2006, Astrophysics Update 2, 285
- Low F. J., Cutri R. M., Kleinmann S. G., & Huchra J. P., 1989, ApJ, 340, L1
- Magorrian J., et al., 1998, AJ, 115, 2285
- Netzer H., et al., 2007, ApJ, 666, 806
- Neugebauer G., Green R. F., Matthews K., Schmidt M., Soifer B. T., & Bennett J. 1987, ApJS, 63, 615
- Neugebauer G., & Matthews K., 1999, AJ, 118, 35
- Rieke G. H., et al., 2004, ApJS, 154, 25
- Rowan-Robinson M., 2000, MNRAS, 316, 885
- Sanders D. B., Soifer B. T., Elias J. H., Madore B. F., Matthews K., Neugebauer G., & Scoville N. Z., 1988, ApJ, 325, 74
- Sanders D. B., & Mirabel I. F., 1996, ARA&A, 34, 749
- Saunders, W., et al. 2000, MNRAS, 317, 55
- Schmidt M., & Green R. F., 1983, ApJ, 269, 352
- Schweitzer M., et al., 2006, ApJ, 649, 79
- Shi Y., et al., 2007, ApJ, 669, 841
- Silk J., Rees M. J., 1998, A&A, 331, L1
- Smith J. D. T., et al., 2007, ApJ, 656, 770
- Spoon H. W. W., Keane J. V., Tielens A. G. G. M., Lutz D., Moorwood A. F. M., & Laurent O., 2002, A&A, 385, 1022
- Spoon H. W. W., Marshall J. A., Houck J. R., Elitzur M., Hao L., Armus L., Brandl B. R., & Charmandaris, V., 2007, ApJ, 654, L49
- Veilleux S., Kim D.-C., & Sanders D. B., 1999, ApJ, 522, 113
- Veilleux S., Kim D.-C., & Sanders D. B., 2002, ApJS, 143, 315
- Voit G. M., Weymann R. J., & Korista, K. T., 1993, ApJ, 413, 95
- Wang J., Wei J. Y., & He X. T., 2006, ApJ, 638, 106
- Wang R., et al., 2007, AJ, 134, 617
- Wang R., et al., 2008, ApJ, in press (arXiv:0806.3022)
- Werner M. W., et al., 2004, ApJS, 154, 1
- Weymann R. J., Turnshek D. A., & Christiansen W. A., 1985, Astrophysics of Active Galaxies and Quasi-Stellar Objects, 333
- Weymann R. J., Morris S. L., Foltz C. B., & Hewett P. C., 1991, ApJ, 373, 23
- Wu H., Zou Z. L., Xia X. Y., & Deng Z. G., 1998, A&AS, 127, 521
- Wu H., Cao C., Hao C.-N., Liu F.-S., Wang J.-L., Xia X.-Y., Deng Z.-G., & Young C. K.-S., 2005, ApJ, 632, L79
- Wu H., Zhu Y.-N., Cao C., & Qin B., 2007, ApJ, 668, 87
- Zheng Z., Wu H., Mao S., Xia X.-Y., Deng Z.-G., & Zou Z.-L., 1999, A&A, 349, 735
- Zheng X. Z., Xia X. Y., Mao S., Wu H., & Den, Z. G., 2002, AJ, 124, 18

**Table 1.** QSO Sample

Object (1)	R.A. (J2000.0) (2)	Decl. (J2000.0) (3)	Redshift (4)	$\log(L_{60\mu\text{m}}/L_{\odot})$ (5)	$\log(L_{\text{opt}}/L_{\odot})$ (6)	SpecType (7)
IR QSOs						
I Zw 1	00 53 34.9	+12 41 36	0.0611	11.310	11.050	S1
F00275–2859	00 30 04.2	–28 42 25	0.2781	12.342	11.568	QSO
3C 48	01 37 41.3	+33 09 35	0.3670	12.648	11.991	QSO
Mrk 1014	01 59 50.2	+00 23 41	0.1630	12.326	11.192	QSO
F02054+0835	02 08 06.8	+08 50 02	0.3450	12.466	11.819	QSO
F07599+6508	08 04 33.1	+64 59 49	0.1483	12.116	11.637	QSO
F11119+3257	11 14 38.9	+32 41 33	0.1890	12.322	12.089	QSO
3C 273	12 29 06.7	+02 03 09	0.1583	12.263	12.427	QSO
Mrk 231	12 56 14.2	+56 52 25	0.0422	12.236	11.467	QSO
F13218+0552	13 24 19.9	+05 37 05	0.2051	12.270	11.467	QSO
F13342+3932	13 36 24.1	+39 17 31	0.1793	12.116	11.821	QSO
F14026+4341	14 04 38.8	+43 27 07	0.3233	12.445	11.930	QSO
PG 1543+489	15 45 30.2	+48 46 09	0.3996	12.344	11.843	QSO
F15462–0450	15 48 56.8	–04 59 34	0.0998	11.995	10.381	S1
PG 1613+658	16 13 57.2	+65 43 10	0.1290	11.533	11.550	QSO
PG 1700+518	17 01 24.8	+51 49 20	0.2920	12.090	12.115	QSO
F18216+6419	18 21 57.3	+64 20 36	0.2970	12.659	12.607	QSO
F20036–1547	20 06 31.7	–15 39 08	0.1919	12.359	11.566	QSO
F21219–1757	21 24 41.6	–17 44 46	0.1120	11.661	10.952	S1
PG QSOs						
PG 0804+761	08 10 58.6	+76 02 42	0.1000	10.794	11.360	QSO
PG 0838+770	08 44 45.2	+76 53 09	0.1310	10.994	11.020	S1
PG 0844+349	08 47 42.4	+34 45 04	0.0640	10.323	10.854	S1
PG 1004+130	10 07 26.1	+12 48 56	0.2408	11.639	11.964	QSO
PG 1119+120	11 21 47.1	+11 44 18	0.0502	10.536	10.509	S1
PG 1149–110	11 52 03.5	–11 22 24	0.0490	10.435	10.299	S1
PG 1211+143	12 14 17.7	+14 03 13	0.0809	11.084	11.414	QSO
PG 1351+640	13 53 15.8	+63 45 45	0.0882	11.248	11.203	QSO
PG 1411+442	14 13 48.3	+44 00 14	0.0896	10.579	10.945	S1
PG 1426+015	14 29 06.6	+01 17 06	0.0865	10.753	11.194	QSO
PG 1444+407	14 46 45.9	+40 35 06	0.2673	11.556	11.636	QSO
PG 1501+106	15 04 01.2	+10 26 16	0.0364	10.468	10.649	S1
PG 1519+226	15 21 14.2	+22 27 43	0.1370	10.963 <sup>a</sup>	11.001	S1
PG 1534+580	15 35 52.3	+57 54 09	0.0296	9.663	10.069	S1
PG 1535+547	15 36 38.3	+54 33 33	0.0389	9.742 <sup>a</sup>	10.530	S1
PG 1552+085	15 54 44.6	+08 22 22	0.1190	10.782 <sup>a</sup>	10.974	S1
PG 1612+261	16 14 13.2	+26 04 16	0.1309	11.053	11.019	S1
PG 1617+175	16 20 11.3	+17 24 28	0.1124	10.637	11.140	QSO
PG 2130+099	21 32 27.8	+10 08 19	0.0630	10.748	10.876	S1

Notes – Basic properties of IR QSOs and PG QSOs in our sample. Col.(1): source name; Col.(2)-(3): right ascension (hours, minutes, seconds) and declination (degrees, arcminutes, arcseconds), from NED; Col.(4): redshift, from NED; Col.(5): monochromatic luminosity at  $60\mu\text{m}$ ; Col.(6): monochromatic luminosity at  $5100\text{\AA}$ ,  $\lambda L_{\lambda}(5100\text{\AA})$ . The values are derived from Hao et al. (2005a) except for F14026+4341 it is measured based on the SDSS spectrum, and for some PG QSOs not included in Hao et al. (2005a) their values were taken from Neugebauer et al. (1987) and calculated in the same manner as in Hao et al. (2005a); Col.(7): optical spectral classifications of IR QSOs (Seyfert 1 or QSO). The typical uncertainties of IR and optical luminosities are about 0.06 dex and 10-20%, respectively (Hao et al. 2005a).

<sup>a</sup>The  $60\mu\text{m}$  flux density is an upper limit.

**Table 2.** ULIRG Sample

Object (1)	R.A. (J2000.0) (2)	Decl. (J2000.0) (3)	Redshift (4)	$\log(L_{60\mu\text{m}}/L_{\odot})$ (5)	$\alpha(60, 25)$ (6)	SpecType (7)
F00188–0856	00 21 26.5	–08 39 26	0.1284	12.166	–2.22	L
F00397–1312	00 42 15.5	–12 56 03	0.2617	12.702	–1.70 <sup>a</sup>	H
F01004–2237	01 02 50.0	–22 21 57	0.1177	12.031	–1.42	H
F01199–2307	01 22 20.9	–22 52 07	0.1560	12.143	–2.62 <sup>a</sup>	H
F01298–0744	01 32 21.4	–07 29 08	0.1362	12.201	–2.49 <sup>a</sup>	H
F01355–1814	01 37 57.4	–17 59 21	0.1920	12.284	–2.36 <sup>a</sup>	H
Z03521+0028	03 54 42.2	+00 37 03	0.1519	12.333	–2.69	L
F05189–2524	05 21 01.5	–25 21 45	0.0426	11.880	–1.57	S2
F08572+3915	09 00 25.4	+39 03 54	0.0584	11.899	–1.68	L
F09463+8141	09 53 00.5	+81 27 28	0.1560	12.093	–3.38 <sup>a</sup>	L
F10091+4704	10 12 16.7	+46 49 43	0.2460	12.451	–3.02 <sup>a</sup>	L
F10378+1108	10 40 29.2	+10 53 18	0.1362	12.167	–2.60	L
F11095–0238	11 12 03.4	–02 54 22	0.1066	12.091	–2.34	L
F11223–1244	11 24 50.0	–13 01 13	0.1990	12.354	–2.61 <sup>a</sup>	S2
F11582+3020	12 00 46.8	+30 04 15	0.2230	12.335	–2.30 <sup>a</sup>	L
F12032+1707	12 05 47.7	+16 51 08	0.2170	12.389	–2.01 <sup>a</sup>	L
F12072–0444	12 09 45.1	–05 01 14	0.1284	12.145	–1.74	S2
F12112+0305	12 13 46.0	+02 48 38	0.0733	12.164	–3.22	L
Mrk 273	13 44 42.1	+55 53 13	0.0378	11.974	–2.57	S2
F13451+1232	13 47 33.3	+12 17 24	0.1217	11.985	–1.20	S2
F14070+0525	14 09 31.2	+05 11 32	0.2644	12.611	–2.15 <sup>a</sup>	S2
F14348–1447	14 37 38.3	–15 00 23	0.0827	12.182	–3.00	L
F15001+1433	15 02 31.9	+14 21 35	0.1627	12.250	–2.76	S2
F15206+3342	15 22 38.0	+33 31 36	0.1244	11.971	–1.86	H
Arp 220	15 34 57.1	+23 30 11	0.0181	12.002	–2.94	H
F16090–0139	16 11 40.5	–01 47 06	0.1336	12.348	–2.99	L
F16300+1558	16 32 21.4	+15 51 45	0.2417	12.532	–2.83 <sup>a</sup>	L
F16333+4630	16 34 52.6	+46 24 53	0.1910	12.207	–2.87 <sup>a</sup>	L
NGC 6240	16 52 58.9	+02 24 03	0.0245	11.608	–2.16	L
F17068+4027	17 08 32.1	+40 23 28	0.1790	12.192	–2.73	H
F17179+5444	17 18 54.2	+54 41 47	0.1470	12.015	–2.18	S2
F20414–1651	20 44 18.2	–16 40 16	0.0871	12.032	–2.90	H
F22491–1808	22 51 49.2	–17 52 23	0.0778	12.024	–2.62	H
F23129+2548	23 15 21.4	+26 04 32	0.1790	12.327	–3.00 <sup>a</sup>	L
F23498+2423	23 52 26.0	+24 40 17	0.2120	12.244	–1.82 <sup>a</sup>	S2

Notes – Basic properties of non-Seyfert 1 ULIRGs in our sample. Col.(1): source name; Col.(2)-(3): right ascension (hours, minutes, seconds) and declination (degrees, arcminutes, arcseconds), from NED; Col.(4): redshift, from NED; Col.(5): monochromatic luminosity at 60 $\mu\text{m}$ ; Col.(6): infrared color index  $\alpha(60, 25)$ ; Col.(7): optical spectral type, derived from Veilleux et al. (1999) and Wu et al. (1998). The typical uncertainty of IR luminosities is about 0.06 dex (Hao et al. 2005a).

<sup>a</sup>The 25  $\mu\text{m}$  flux density is an upper limit.

**Table 3.** IRS Observation Log of IR QSOs

Object (1)	SL (2)	LL (3)	PID (L) (4)	SH (5)	LH (6)	PID (H) (7)
I Zw 1	2×14.68	2×14.68	14	4×31.46	2×60.95	14
F00275−2859	2×60.95	2×31.46	105	3×121.9	8×60.95	1096
3C 48	1×6.29	1×14.68	82	...	...	...
Mrk 1014	3×14.68	2×31.46	105	6×31.46	4×60.95	105
F02054+0835	2×60.95	2×31.46	105	...	...	...
F07599+6508	3×14.68	2×31.46	105	6×31.46	4×60.95	105
F11119+3257	1×60.95	3×31.46	105	3×121.9	4×60.95	105
3C 273	3×14.68	3×14.68	105	6×31.46	4×60.95	105
Mrk 231	2×14.68	5×6.29	105	6×31.46	4×60.95	105
F13218+0552	1×60.95	3×31.46	105	3×121.9	4×60.95	105
F13342+3932	2×60.95	2×31.46	105	3×121.9	2×241.83	105
F14026+4341	7×14.68	7×14.68	61	14×121.9	28×60.95	61
PG 1543+489	2×60.95	2×121.9	20142	...	...	...
F15462−0450	1×60.95	3×31.46	105	3×121.9	4×60.95	105
PG 1613+658	2×60.95	2×121.9	3187 & 20142	3×121.9	10×241.83	3187
PG 1700+518	1×6.29	1×14.68	82	2×121.9	7×241.83	3187
F18216+6419	1×14.68	1×31.46	82	3×121.9	3×241.83	3746
F20036−1547	2×60.95	2×31.46	105	...	...	...
F21219−1757	2×60.95	...	3187	2×121.9	2×241.83	3187

Notes – The integration times for each slit are given. The quantity is the number of DCEs “×” ramp time (in sec) for a single nod. Col.(1): source name; Col.(2)-(4): integration times and program IDs for the low-resolution (short-low [SL] & long-low [LL] modes) observations; Col.(5)-(7): integration times and program IDs for the high-resolution (short-high [SH] & long-high [LH] modes) observations.



**Table 4.** IRS Observation Log of PG QSOs and ULIRGs

Object (1)	SL (2)	PID (SL) (3)	LL (4)	PID (LL) (5)
PG QSOs				
PG 0804+761	3×14.68	14	2×31.46	14
PG 0838+770	2×241.83	3187	2×121.9	20142
PG 0844+349	2×60.95	3187	2×121.9	20142
PG 1004+130	2×60.95	20142	2×121.9	20142
PG 1119+120	3×14.68	14	2×31.46	14
PG 1149−110	2×60.95	20142	2×121.9	20142
PG 1211+143	3×14.68	14	2×31.46	14
PG 1351+640	3×14.68	14	2×31.46	14
PG 1411+442	2×60.95	3187	1×121.9	3421
PG 1426+015	2×60.95	3187	2×121.9	20142
PG 1444+407	2×60.95	20142	2×121.9	20142
PG 1501+106	3×14.68	14	2×31.46	14
PG 1519+226	2×60.95	20142	2×121.9	20142
PG 1534+580	2×60.95	20142	2×121.9	20142
PG 1535+547	3×60.95	3421	1×121.9	3421
PG 1552+085	2×60.95	20142	2×121.9	20142
PG 1612+261	2×60.95	20142	2×121.9	20142
PG 1617+175	3×60.95	3187	2×121.9	20142
PG 2130+099	3×14.68	14	2×31.46	14
ULIRGs				
F00188−0856	2×60.95	105	3×31.46	105
F00397−1312	2×60.95	105	3×31.46	105
F01004−2237	1×60.95	105	2×31.46	105
F01199−2307	2×60.95	105	3×31.46	105
F01298−0744	2×60.95	105	2×31.46	105
F01355−1814	2×60.95	105	2×31.46	105
Z03521+0028	2×60.95	105	3×31.46	105
F05189−2524	3×14.68	105	2×14.68	105
F08572+3915	3×14.68	105	3×14.68	105
F09463+8141	2×60.95	105	2×31.46	105
F10091+4704	2×31.46	105	2×31.46	105
F10378+1108	2×60.95	105	3×31.46	105
F11095−0238	2×60.95	105	2×31.46	105
F11223−1244	2×60.95	105	3×31.46	105
F11582+3020	2×60.95	105	2×31.46	105
F12032+1707	2×60.95	105	2×31.46	105
F12072−0444	1×60.95	105	2×31.46	105
F12112+0305	3×14.68	105	2×31.46	105
Mrk 273	2×14.68	105	2×14.68	105
F13451+1232	3×14.68	105	2×31.46	105
F14070+0525	2×60.95	105	2×31.46	105
F14348−1447	1×60.95	105	2×31.46	105
F15001+1433	2×60.95	105	3×31.46	105
F15206+3342	1×60.95	105	3×31.46	105
Arp 220	3×14.68	105	5×6.29	105
F16090−0139	1×60.95	105	3×31.46	105
F16300+1558	2×60.95	105	5×31.46	105
F16333+4630	2×60.95	105	2×31.46	105
NGC 6240	2×14.68	105	2×14.68	105
F17068+4027	2×60.95	105	3×31.46	105
F17179+5444	2×60.95	105	3×31.46	105
F20414−1651	1×60.95	105	2×31.46	105
F22491−1808	1×60.95	105	2×31.46	105
F23129+2548	3×60.95	105	5×31.46	105
F23498+2423	2×60.95	105	2×31.46	105

Notes – The integration times for each slit are given. The quantity is the number of DCEs “×” ramp time (in sec) for a single nod. Col.(1): source name; Col.(2)-(3): integration times and program IDs for the short-low (SL) mode observations; Col.(4)-(5): integration times and program IDs for the long-low (LL) mode observations.

**Table 5.** Mid-IR properties of IR QSOs

Object (1)	S <sub>15</sub> (mJy) (2)	S <sub>30</sub> (mJy) (3)	PAH 6.2 $\mu$ m (10 <sup>-21</sup> W cm <sup>-2</sup> ) (4)	EW(PAH) ( $\mu$ m) (5)	[NeII]12.81 $\mu$ m (10 <sup>-21</sup> W cm <sup>-2</sup> ) (6)
I Zw 1	553.6	1186.0	17.2	0.011	2.87
F00275-2859	93.9	249.7	7.36	0.028	1.29
3C 48	75.6	283.8 <sup>a</sup>	<7.2	<0.051	...
Mrk 1014	225.9	1191.3	12.9	0.048	5.94
F02054+0835	127.8	260.6 <sup>a</sup>	<4.0	<0.018	...
F07599+6508	285.2	754.9	5.85	0.004	3.29
F11119+3257	188.1	645.6	7.52	0.014	2.83
3C 273	336.7	410.4	<9.4	<0.004	1.26
Mrk 231	3385.6	13241.2	81.8	0.012	18.24
F13218+0552	288.1	734.2	6.80	0.005	1.34
F13342+3932	101.7	373.1	16.1	0.089	5.26
F14026+4341	140.0	267.0 <sup>a</sup>	4.45	0.012	0.84
PG 1543+489	69.2	125.3 <sup>a</sup>	<6.1	<0.034	...
F15462-0450	140.7	913.8	23.2	0.099	8.13
PG 1613+658	127.1	261.0	7.80	0.020	4.07
PG 1700+518	122.8	246.6 <sup>a</sup>	<9.5	<0.022	2.09
F18216+6419	240.8	365.4 <sup>a</sup>	<8.1	<0.015	3.82
F20036-1547	95.9	441.4	12.0	0.046	...
F21219-1757	...	...	8.47	0.018	1.71

Notes – Mid-IR spectral properties of IR QSOs. Col.(1): source name; Col.(2)-(3): Continuum flux densities around 15 and 30 $\mu$ m rest wavelength, the uncertainties of the measurements are typically 10%; Col.(4)-(5): Flux and equivalent width (EW) of PAH emissions at 6.2 $\mu$ m, upper limits (3 $\sigma$ ) are derived adopting widths of 0.2 $\mu$ m; Col.(6) fluxes of [NeII] 12.81 $\mu$ m line.

<sup>a</sup>Outside the rest wavelength range available, the value given here was linearly extrapolated based on the logarithm of the  $\sim 25\mu$ m rest wavelength continuum level.

**Table 6.** Mid-IR properties of PG QSOs and ULIRGs

Object (1)	S <sub>15</sub> (mJy) (2)	S <sub>30</sub> (mJy) (3)	PAH 6.2 $\mu$ m (10 <sup>-21</sup> W cm <sup>-2</sup> ) (4)	EW(PAH) ( $\mu$ m) (5)
PG QSOs				
PG 0804+761	125.5	150.8	<7.4	<0.012
PG 0838+770	45.4	97.4	<2.0	<0.026
PG 0844+349	105.5	155.1	<6.5	<0.018
PG 1004+130	72.9	118.5	<2.0	<0.014
PG 1119+120	176.9	303.9	<2.1	<0.008
PG 1149-110	140.3	249.6	<2.1	<0.019
PG 1211+143	239.6	268.8	<7.5	<0.014
PG 1351+640	249.4	536.2	10.9	0.034
PG 1411+442	125.3	143.2	<4.2	<0.010
PG 1426+015	136.1	181.2	<5.2	<0.013
PG 1444+407	69.8	99.1	<7.54	<0.036
PG 1501+106	297.6	424.9	<3.4	<0.008
PG 1519+226	54.2	70.8	2.46	0.016
PG 1534+580	107.2	149.1	<2.08	<0.008
PG 1535+547	98.4	111.5	<3.1	<0.011
PG 1552+085	79.7	94.2	<1.3	<0.017
PG 1612+261	83.4	136.4	<3.0	<0.020
PG 1617+175	53.8	65.7	<3.2	<0.020
PG 2130+099	196.4	293.0	3.56	0.006
ULIRGs				
F00188-0856	122.8	1052.7	27.5	0.187
F00397-1312	90.1	523.5	9.14	0.018
F01004-2237	306.4	1176.4	11.2	0.048
F01199-2307	39.1	455.0	3.75	0.146
F01298-0744	65.4	718.5	7.53	0.092
F01355-1814	27.7	369.6	<2.7	<0.186
Z03521+0028	50.6	980.1	20.9	1.086
F05189-2524	1017.6	4994.1	54.8	0.034
F08572+3915	657.6	3272.9	<7.7	<0.004
F09463+8141	9.0	193.3	7.61	1.483
F10091+4704	13.3	197.1	7.06	0.758
F10378+1108	48.5	571.9	11.0	0.415
F11095-0238	111.8	1112.0	<3.7	<0.025
F11223-1244	19.0	214.3	<2.2	<0.065
F11582+3020	32.5	352.8	1.25	0.022
F12032+1707	45.5	428.8	<7.1	<0.161
F12072-0444	197.3	878.6	13.6	0.106
F12112+0305	106.4	1683.5	56.8	0.431
Mrk 273	416.1	5068.8	74.8	0.129
F13451+1232	286.5	996.7	<3.0	<0.013
F14070+0525	21.6	304.0	5.59	0.187
F14348-1447	82.7	1309.2	33.5	0.365
F15001+1433	59.6	475.1	16.1	0.184
F15206+3342	101.6	628.9	38.2	0.342
Arp 220	1048.1	20907.7	161.0	0.272
F16090-0139	76.5	808.3	13.5	0.107
F16300+1558	25.7	490.4	11.0	0.282
F16333+4630	20.2	260.9	12.5	0.529
NGC 6240	752.1	5763.0	313.0	0.365
F17068+4027	52.3	410.9	10.8	0.198
F17179+5444	72.6	341.8	6.43	0.099
F20414-1651	61.7	1397.4	37.5	0.587
F22491-1808	82.9	1473.3	23.1	0.465
F23129+2548	40.2	434.9	<1.1	<0.021
F23498+2423	46.4	239.7	6.11	0.053

Notes – Mid-IR spectral properties of PG QSOs and ULIRGs in our sample. The definition of columns is the same as in Table 5.